Princeton Plasma Physics Laboratory

PPPL- 4521

PPPL- 4521

Imaging with Spherically Bent Crystals or Reflectors

M. Bitter, L.F. Delgado Apricio, K.W. Hill, S. Scott, A. Ince-Cushman,
M. Reinke, Y. Podpaly, J.E. Rice, P. Beiersdorfer, and E. Wang

June, 2010

Prepared for the U.S. Department of Energy under Contract DE-AC02-09CH11466.

Princeton Plasma Physics Laboratory
Report Disclaimers

Full Legal Disclaimer

Trademark Disclaimer

PPPL Report Availability

Princeton Plasma Physics Laboratory:

http://www.pppl.gov/techreports.cfm

Office of Scientific and Technical Information (OSTI):

http://www.osti.gov/bridge

Related Links:

U.S. Department of Energy

Office of Scientific and Technical Information

Fusion Links

000

Imaging with Spherically bent Crystals or Reflectors

M. Bitter, L. F. Delgado Aparicio, K. W. Hill, S. Scott,
Princeton University, Plasma Physics Laboratory, Princeton, NJ 08543,USA

A. Ince-Cushman, M. Reinke, Y. Podpaly, J. E. Rice
Plasma Science and Fusion Center, Massachusetts Institute of Technology, Cambridge, MA 02139, USA

P. Beiersdorfer, and E. Wang
Lawrence Livermore National Laboratory, Livermore, CA 94550, USA

E-mail: bitter@pppl.gov

Abstract.

This paper consists of two parts: *Part I* describes the working principle of a recently developed x-ray imaging crystal spectrometer, where the astigmatism of spherically bent crystals is being used with advantage to record spatially resolved spectra of highly charged ions for Doppler measurements of the ion-temperature and toroidal plasma-rotation-velocity profiles in tokamak plasmas. This type of spectrometer was thoroughly tested on NSTX and Alcator C-Mod, and its concept was recently adopted for the design of the ITER crystal spectrometers. *Part II* describes imaging schemes, where the astigmatism has been eliminated by the use of matched pairs of spherically bent crystals or reflectors. These imaging schemes are applicable over a wide range of the electromagnetic radiation, which includes microwaves, visible light, EUV radiation, and x-rays. Potential applications with EUV radiation and x-rays are the diagnosis of laser-produced plasmas, imaging of biological samples with synchrotron radiation, and lithography.

I. Introduction

We recently developed a x-ray imaging crystal spectrometer for Doppler measurements of the ion-temperature and toroidal rotation-velocity profiles in tokamak plasmas [1, 2], where the astigmatism of a spherically bent crystal is being used with advantage to produce a one-dimensional image of the plasma and to record spectra of highly charged ions with high spatial as well as high temporal and high spectral resolution. A longstanding problem for the x-ray spectroscopy of tokamak plasmas was thereby solved, since the x-ray crystal spectrometers, used in the past, had no spatial resolution and provided spectra from only one sightline through the plasma. Arrays of several such single-chord instruments were used on TFTR and Alcator C-Mod to obtain some information on the radial profiles of the ion temperature [3-6]. But since x-ray spectrometers for Doppler measurements are large, only a few spectrometers could be fielded in those tokamak experiments, so that only a few points of the radial ion-temperature profiles were obtained. The x-ray spectroscopy was, therefore, with respect to the measurement of ion-temperature profiles, not competitive with the charge exchange recombination spectroscopy [7], which employs emission lines in the visible spectral range, where optical instrumentation and well established imaging methods can be used to obtain radial profiles with high spatial resolution. The charge exchange recombination spectroscopy is today the main diagnostic for ion temperature measurements on tokamak experiments, but it may not be applicable as a core ion temperature diagnostic on future large tokamaks, such as ITER, due to the fact that neutral hydrogen beams, which are a key requirement for the operation of this diagnostic, may not penetrate to the center of the plasma. The x-ray spectroscopy of highly charged ions has, therefore, become an attractive alternative for the diagnosis of the core ion temperature as well as for measurements of the ion temperature profile on ITER. Of particular interest for these measurements are the Kα lines of the helium-like ions of medium-Z elements from argon through krypton and the L-shell spectra of neon-like tungsten, which will be an intrinsic impurity on ITER. The requirements with respect to the spatial resolution of the ion-temperature profile measurements on ITER will be met

by appropriately designed x-ray imaging spectrometers [8]. In this paper we describe the working principle of our x-ray imaging crystal spectrometers, which were thoroughly tested on NSTX and Alcator C-Mod. We mention that spectrometers with spherically or toroidally bent crystals are also being used for the diagnosis of laser produced plasmas [9-12], and we point out that the instrumental requirements and spectrometer designs for the diagnosis of small laser-produced plasma sources and Doppler measurements of the ion temperature and rotation velocity profiles in extended tokamak plasma sources are very different. The differences reside not only in the spectrometer dimensions and layouts, and the detectors used (to obtain high throughput as well as high time and spatial resolution for the duration of a plasma discharge of several seconds) but also in the fact that the astigmatism of the spherically bent crystal can be used with advantage because of the symmetry due to the toroidal magnetic field and uniformity of the x-ray emission along the toroidal magnetic field. We also present supplementary information on imaging schemes, where the astigmatism has been eliminated by the use of matched pairs of spherically bent crystals or reflectors [13, 14]. These imaging schemes, which are still in the early stages of development and testing, should be applicable to a wide spectrum of the electromagnetic radiation. Potential applications with EUV radiation and x-rays are the diagnosis of laser-produced plasmas, imaging of biological samples with synchrotron radiation, and lithography.

II. Working principle of a x-ray imaging crystal spectrometer for Doppler measurements of the ion temperature and toroidal plasma rotation velocity profiles in tokamak plasmas.

The imaging properties of a spherically bent crystal and the preferred arrangement in tokamak experiments are illustrated in Fig. 1. The working principle can be readily understood if one assumes that the ray pattern produced by a small source at the point P on the Rowland circle. The source is at a distance $R \bullet \sin(\theta)$ from the center of the crystal, where R is the radius of curvature of the crystal and θ a certain Bragg angle. The dimensions of the source are assumed to be of the order of the Johann focusing error,

$\Delta_J = \frac{l^2 \bullet \cos(\theta)}{8 \bullet R}$, where l is the length of the crystal [15], in order to assure that the source can deliver all the rays, which impinge at any point on the crystal surface with the Bragg angle θ. Since the Johann error Δ_J is usually small and of the order of the detector resolution, the source can still be considered as a quasi point source, and the point P can, therefore, be associated with the Bragg angle θ and a wavelength λ, given by the Bragg condition. Because of the astigmatism of spherical mirrors, a distinction must be made between the *meridional* and *sagittal* rays, which are governed by different image equations (Coddington's equations [16]) and which are shown in Fig. 1 in red and blue colors, respectively. The imaging equations for the *meridional* and *sagittal* rays are

$$(1) \qquad \frac{1}{a} + \frac{1}{b_m} = \frac{2}{R \bullet \sin(\theta)}$$

and

$$(2) \qquad \frac{1}{a} + \frac{1}{b_s} = \frac{2 \bullet \sin(\theta)}{R}$$

where a, b_m, and b_s are the distances of the object and the *meridional* and *sagittal* images, at B_m and B_s, from the center of the crystal. Inserting $a = R \bullet \sin(\theta)$ in equations (1) and (2), one obtains

$$(3) \qquad b_m = R \bullet \sin(\theta)$$

for the *meridional* rays, and

$$(4) \qquad b_s = -\frac{b_m}{\cos(2\theta)}$$

for the *sagittal* rays. The images at B_m and B_s are produced by rays reflected from a small central crystal element at C. The images, obtained from an arbitrary crystal element, can easily be identified from symmetry operations on the triangle $B_s(O)PC$: The *meridional* rays can be traced by rotating the triangle $B_s(O)PC$ about an axis perpendicular to the plane of the Rowland circle passing through O. If such a rotation is performed, the point

C slides on the spherical crystal surface, and the points B_m and B_s describe circles about O with the radii $R \bullet \cos(\theta)$ and $\frac{R \bullet \cos(\theta)}{-\cos(2\theta)}$, respectively. Similarly, the image formation by the *sagittal* rays can be visualized by a rotation of the triangle $B_s(O)PC$ about the axis $B_s(O)P$ in the plane of the Rowland circle, whereby the points P, O, and B_s remain fixed and the point C moves up or down on the spherical crystal surface, and where the sides PC and CP of the triangle $B_s(O)PC$ represent the incident and reflected rays, respectively. The formation of the two, mutually perpendicular line-images near B_m and B_s can thus be understood as a result of these symmetries.

The location of the *sagittal* line-image depends on the Bragg angle θ and is determined by equation (4). One can distinguish the following cases:

(a) For $\theta > 45°$, $b_s > 0$, the reflected *sagitta*l rays converge to a real *sagittal* line-image at B_s in front of the crystal as depicted in Fig. 1.

(b) For $\theta = 45°$, $b_s = \infty$, the *sagittal* image B_s is at infinity and the reflected *sagittal* rays are parallel.

(c) For $\theta < 45° \; b_s < 0$, the reflected *sagittal* rays are divergent and seem to originate from a *virtual sagittal* line-source at a point B_s behind the crystal.

Since the light path can be reversed, Fig. 1 also describes the formation of a point image at P of a line-source at B_s. This image can be recorded by placing a two-dimensional detector at P. The ray pattern shown in Fig. 1 is symmetric with respect to a rotation about the axis OC, which is normal to the surface of the spherical crystal at the point C. If the ray pattern is rotated about OC, the points B_s and S move on opposite sites of a cone with the axis OC, whereby the trace of the point P in the detector plane describes a conic section. The type of this conic section is determined by the orientation of the detector plane. It is, in most cases, an ellipse. Each point of such an ellipse in the detector

is associated with a line-source above or below the plane of the Rowland circle, so that the points of the ellipse represent the spatially resolved images of those line sources. The ellipse is also associated with a certain wavelength λ, since the ray pattern shown in Fig. 1 refers to a certain Bragg angle θ.

The experimental arrangement, shown in Fig. 1, where the *sagittal* line source is parallel to the toroidal magnetic field lines, is the preferred arrangement of the crystal spectrometer on tokamaks, since the electron density, electron temperature, and, therefore, the x-ray emissivity are uniform along the toroidal magnetic field. The finite extension of the *sagittal* line-source due to the astigmatism of a spherical crystal is then of no concern. It is due to this toroidal symmetry of tokamak plasmas that the astigmatism of spherically bent crystals can be used with advantage to obtain a one-dimensional image of the plasma with spatial resolution in the direction perpendicular to the toroidal magnetic field.

The spatial resolution obtained in the plasma is determined by the height of the crystal, the Bragg angle, and position of the line-source relative to the plasma. For $\theta = 45°$, the spatial resolution is solely determined by the height of the crystal, since B_s is then at infinity, so that the *sagittal* rays, incident on the crystal, are parallel.

X-ray imaging crystal spectrometers, with the here-described working principle, are now operating on NSTX [17], EAST [18], KSTAR [19], and Alcator C-Mod [2, 20-22]. The spectrometer on Alcator C-Mod is the most advanced instrument, since it incorporates two spherically bent 102-quartz crystals, with a 2d-spacing of 4.56216 Å and radii of curvature of 144.3 cm and 138.5 cm, for observation of the spectra of helium-like and hydrogen-like argon, and since it is equipped with four high count rate Pilatus detector modules. The Pilatus detector modules are based on the modern CMOS hybrid-pixel technology [23, 24]. Each module has a sensitive area of 83.8 x 33.5 mm^2, which comprises 94,965 pixels with a pixel seize of 172 x 172 μm^2. Very important features are the high single-photon count rate capability 2 MHz per pixel and low neutron response. These detector modules are radiation hardened and have been tested with neutron

fluences up to $10^{14}$and 10^{15} neutrons/cm^{2}s^1. Shielding of these detectors is not required on present facilities like NSTX, where the background due to neutrons and gammas of the order of 200 counts per pixel and second is negligible against the typical x-ray counts of 10^4 photons per pixel and second.

The x-ray imaging crystal spectrometer on Alcator C-Mod, which is in operation since April 2007, has provided spatially and temporally resolved data on the ion temperature and toroidal plasma rotation velocity from plasmas with Ohmic heating, RF heating, and lower-hybrid current drive. A detailed description of the instrument and results obtained for various experimental conditions have been published in refs. [2, 20-22, 25-29]. In this paper, the attention is focused on basic experimental results, which verify the here-described imaging properties.

The essential features of the x-ray imaging crystal spectrometer, which is used on Alcator C-Mod for observation of the spectra of helium-like argon, are shown in Fig. 2. This spectrometer employs three Pilatus detector modules. They are arranged on a cone and record an image of the entire, 72 cm high, elongated plasma cross-section with a de-magnification of 2.6, given by the ratio of the 296 cm long distance from the crystal to the center of the plasma and the 113 cm long distance between crystal and detector. The elliptical curves seen on the detector modules represent the main spectral lines of helium-like argon: $1s^2\ ^1S_0 - 1s2p\ ^1P_1$ (**w**), $1s^2\ ^1S_0 - 1s2p\ ^3P_2$ (**x**), $1s^2\ ^1S_0 - 1s2p\ ^3P_1$ (**y**), and $1s^2\ ^1S_0 - 1s2s\ ^3S_1$ (**z**) at the wavelengths of 3.9494 Å, 3.9661 Å, 3.9695 Å, and 3.9944 Å, respectively, and the associated, dielectronic and/or collisionally excited, lithium-like satellites [30-32]. The wavelength is displayed along the short dimension of the Pilatus detector modules, increasing from left to right, and the spatial information is displayed along the long dimension of the Pilatus detector modules. An, at first, surprising result was the observation of faint helium-like lines, **w**, **x**, **y**, and **z** and absence of satellites in the spectra, recorded on the two outer detector modules from the cold edge of the plasma. These spectra must be ascribed to the recombination of hydrogen-like argon, since the edge electron temperature is too low for the direct (electron impact) excitation of the helium-like lines from the helium-like ground state and the excitation of the dielectronic

and collisionally excited lithium-like satellites. The helium-like lines are also very narrow due to the absence of the unresolved $n \geq 3$ dielectronic satellites, and they are therefore well suited for measurements of the ion temperature in the cold edge of the plasma. The range for ion temperature and plasma rotation velocity measurements is thereby significantly extended. The spectral lines are found on ellipses with the theoretically predicted parameters, so that imaging properties of the spherically bent crystal have been verified by these experimental results.

Figures 3 and 4 present the spectral data from the Alcator C-Mod discharge, 1070614011, which had a plasma current of 800 kA and additional RF heating of 3 MW during the time interval from 0.7 to 1.2 s. The central electron temperatures obtained during the time intervals of Ohmic and RF heating were 1.6 and 4.0 keV, respectively. Figure 3 shows spatially resolved spectra of helium-like argon, recorded at the time of $t = 0.917s$, as a function of the vertical plasma coordinate z, in the range from $z = -30cm$ to $z = +30cm$. We infer from Fig. 3 that the emissivity profiles of the helium-like lines **w**, **x**, **y**, and **z** are hollow in the center of the plasma due to the fact that helium-like ions are ionized to the hydrogen-like charge state. Figure 4 shows the helium-like argon spectra observed from the same discharge at the fixed position $z = -0.68cm$, near the center of the plasma, as a function of time. It is evident from Fig. 4 that the intensities of the helium-like lines **w**, **x**, **y**, and **z** increase strongly at the beginning of the RF heating at 0.7 s; decrease as the central electron temperature reaches values of $T_e = 4.0keV$; increase again at the end of the RF heating pulse during the time interval from 1.2 to 1.5 s due to the recombination of the hydrogen-like argon ions; and then decrease at the end of the discharge during the time interval from 1.8 to 2.5 s, when the central electron temperature is less than 0.5 keV. During this last time interval, the helium-like lines can only be excited by the recombination of hydrogen-like argon. Variations of the line positions and line widths with time and plasma coordinate z are already noticeable by eye in Figs. 3 and 4.

The chord-integrated x-ray line spectra, shown in Figs. 2, 3 and 4 can be inverted to obtain the local ion temperature and local plasma rotation velocities. The spatial resolution in the plasma in the vertical direction is $\Delta z = 5mm$. It is determined by the

dimensions of the 27 mm high and 64 mm wide crystal, its radius of curvature of 144.3 cm, the mean Bragg angle of 60.5°, and the distance of 296 cm between the crystal and the center of the plasma. The spatial resolution in the plasma of $\Delta z = 5mm$ corresponds to $\approx 2mm$ or 12 column pixels on the detector, since the de-magnification of the image is 2.6. The spectra are usually analyzed by adding the counts in 30 adjacent vertical column pixels, which corresponds to the accumulation of the spectral data from a $\approx 13mm$ high plasma segment. Since the number of column pixels per Pilatus detector module is 487, one obtains 16 bins of 30 column pixels per Pilatus detector module and a total of 48 column bins for the three Pilatus modules, which represent 48 sightlines through the plasma. The typically observed count rate at the peak of the **w**-line is 10^4 photons per pixel and sec, and since the width of the **w**-line at FWHM is about 5 pixels, one obtains 25,000 photons per sec in a horizontal row of pixels for the **w**-line. The count rate for the **w**-line per sightline is, therefore, 30 x 25,000 = 7.5 x 10^5 photons per sec, or 7.5 x 10^3 photons per 10 ms, so that the statistical error for the data collected per sightline in 10 ms time intervals is about 1% and sufficiently small for an inversion of the data. The techniques developed by I. Condrea and R. Bell [33-35] are presently used for the tomographic inversion of the spectral data [2]. New inversion software, which will take into account effects of the Johann error and other instrumental characteristics, is in preparation.

We point out that the dimensions and layout of the x-ray crystal spectrometers for ITER will be very similar to the dimensions and layout of the spectrometer on Alcator C-Mod, so that this instrument on Alcator C-Mod can be considered as a prototype for the crystal spectrometers on ITER. Recent neutronics calculations [36] have shown that the Pilatus detector modules will survive the harsh neutron an gamma background on ITER with feasible shielding.

III. Imaging schemes with matched pairs of spherically bent crystals or reflectors.

Although the astigmatism of a spherically bent crystal can be used with advantage for one-dimensional imaging of tokamak plasmas and measurements of the ion temperature and rotation velocity profiles, it is an unwelcome imaging error in most cases, where a direction of symmetry is absent and a stigmatic two-dimensional imaging of an object is required. In those cases, schemes of near-paraxial rays are often applied to minimize astigmatic image distortions. To alleviate these constraints, we have recently proposed new imaging schemes, where the astigmatism is eliminated by the use of matched pairs of spherically bent crystals or reflectors [14, 15], so that stigmatic imaging can be obtained for almost arbitrary angles of incidence. Proposals of different schemes to eliminate the astigmatism have been made by MissalIa et al. [11], Podorov et al. [12], and Gardner [37]. In this section, we discuss the differences between our schemes and those schemes and derive the equations, which determine the relevant instrumental parameters of our schemes.

The imaging schemes shown in Figs. 5 and 6 represent the two cases, where the Bragg angles for the incident rays on the spherical mirrors, mirror-1 and mirror-2, are $0° < \theta_1 < 45°$, $45° < \theta_2 < 90°$ and $45° < \theta_1 < 90°$, $45° < \theta_2 < 90°$, respectively. The first imaging scheme, shown in Fig. 5, produces a point image at I of a point source at P, where P and I are located on the Rowland circles of the two mirrors (or crystals), at the distances $R_1 \sin(\theta_1)$ and $R_2 \sin(\theta_2)$ from C_1 and C_2, respectively. This imaging scheme works as follows: The rays emanating from P strike mirror-1 under a Bragg angle $\theta_1 < 45°$, so that they form a virtual *sagittal* line image of the point source in the plane of dispersion (drawing plane) through the point B_{s1} behind mirror-1 and a real *meridional* line image, perpendicular to the plane of dispersion, at B_{m1} in front of mirror-1. The *sagittal* rays reflected from mirror-1 are, therefore, divergent and seem to emanate from the virtual *sagittal* line source at B_{s1}, while the reflected *meridional* rays converge at B_{m1}. In order to obtain a point image at I the radius of curvature R_2 of mirror-2 and Bragg angle $\theta_2 > 45°$ must be appropriately chosen such that the real *meridional* and *sagittal* images, which would be produced by mirror-2 of a point source at I, coincide with the real *meridional* image and virtual *sagittal* image produced by mirror-1. As pointed out in ref. [13], the necessary condition is

$$(8) \qquad b_{m1} + b_{m2} = b_{s1} + b_{s2} = d$$

where b_{m1}, b_{s1}, and b_{m2}, b_{s2} are the distances of the *meridional* and *sagittal* images from C_1 and C_2, respectively, and where d is the distance between the two mirrors. - Note that b_{s1} is negative. For the arrangement shown in Fig. 5, with P and I located on the Rowland circles of mirror-1 and mirror-2, this condition can be expressed as

$$(9) \qquad R_1 \cos(\theta_1) \bullet \tan(2\theta_1) = -R_2 \cos(\theta_2) \bullet \tan(2\theta_2)$$

The total magnification of this scheme is $M = M_1 \bullet M_2 = 1$, where $M_1 = \frac{b_{m1}}{a} = 1$ and $M_2 = \frac{b_{m2}}{a} = 1$ and where a, b_{m1}, and b_{m2} are the distances of P and I and the corresponding *meridional* images from the center of mirror-1 and mirror-2, respectively.

The second imaging scheme, shown in Fig. 6, is obtained from Fig. 1 if the rays, which emerge from the *sagittal* line source at B_s and form a point image at P, are extended beyond P and allowed to be reflected from a second spherically bent reflector at C_2 to form a real *sagittal* line image at B_{s2}. The *sagittal* line image at B_{s2} is a stigmatic image of the *sagittal* line source at B_{s1}. The Bragg angles are $\theta_1 > 45°$ and $\theta_2 > 45°$, so that the two sagittal line image (source) at $B_{s1}(B_{s2})$ are both real. The total magnification is $M = \frac{\cos(2\theta_2)}{\cos(2\theta_1)}$ [14].

The two imaging schemes, presented in Figs. 5 and 6, should be applicable to a broad spectrum of the electromagnetic radiation, which includes microwaves and visible light as well as EUV radiation and x-rays. However, for EUV radiation and x-rays, the Bragg condition must be satisfied with both reflectors and the additional condition

$$(10) \qquad R_1 \cos(\theta_1) = R_2 \cos(\theta_2) = RT$$

must be fulfilled to assure that the Johann errors for both reflectors are exactly equal [14]. As shown in Figs. 5 and 6, the centers of the two crystal spheres must be at the same point O, and all the rays must be tangential to a circle about O with the radius RT. The additional condition (10) implies that only the mirror orientations, shown in Figs. 5 and 6, can be used for EUV radiation and x-rays (whereas for other radiations, where the Bragg condition does not need to be satisfied, the second mirror can also be rotated by an angle $180° - 2\theta_2$) and that, for the imaging scheme shown in Fig. 5, the sum of the Bragg angles must be equal to $\theta_1 + \theta_2 = 90°$, since the two conditions, (9) and (10), must be satisfied simultaneously.

We note that the somewhat peculiar ray pattern of the imaging scheme shown in Fig. 6 arises naturally for x-rays and EUV radiation due to the Bragg condition, whereas for other radiations, where the Bragg condition does not need to be satisfied, a vertical slit has to be installed at B_{m1} or B_{m2} in order to establish this ray pattern.

The imaging schemes proposed in refs [ ] are quite different from those described here and in refs [,]. In the following paragraphs we discuss these differences in more detail. Missalla et al. [ ] proposed to eliminate the astigmatism for a particular Bragg angle θ by the use of a toroidally bent mirror, where the ratio of the vertical and horizontal radii of curvature is $\frac{R_v}{R_h} = \sin^2(\theta)$, so that the focal lengths for the meridional and sagittal rays are equal: $f_h = \frac{R_h}{2}\sin(\theta) = \frac{R_v}{2\sin(\theta)} = f_v$. Yet Podorov et al. [ ] pointed out that 'as a rule the x-ray images obtained with one toroidally bent crystal have different sorts of aberrations', and they showed by modeling calculations that these aberrations cause significant image distortions if the magnification, given by $M = \frac{b}{p}$ where p and b are the distances of object and image from the crystal, assumes values outside the narrow interval of $0.9 < M < 1.1$. They further report that the aberrations or coma are generally found on

one side of the central ray and that the coma changes its orientation and its position, moving from one side to the other side of the central ray, as M is varied between 0.9 and 1.1, so that it is possible to minimize the distortions for $M = 0.96$ [ ]. In order to obtain large magnifications of $M = 25$, Podorov et al. proposed an 'optimized two-crystal arrangement', which consists of a concave toroidally bent crystal with large radii of curvature and a magnification of $M \approx 1$ and a convex toroidally bent crystal with relatively small radii of curvature and a large magnification of $M \approx 25$. The authors conclude from their modeling calculations that for a system with a total magnification $M = 25$ the size of the image distortions seen on the detector would be about $75nm$, so that a resolution of $3nm$ could be obtained. We point out that these modeling results were obtained for a Bragg angle of $83°$, i. e. for a case not far from normal incidence. It is also noteworthy that the authors claim that "Spherically bent crystals cannot in principle be used in this arrangement (meaning an arrangement with a Bragg angle far from 90°) because they have different focusing lengths in the diffraction (meridian) and sagittal planes.", a statement which leads us to believe that the authors may not have been aware of the solutions considered in the present paper. Their results about image distortions in two-crystal imaging systems with large magnifications could, however, be relevant for the here considered imaging systems of spherical mirrors.

Another imaging scheme, which has to be discussed here, was proposed by J. L. Gardner in an article entitled 'Astigmatism Cancellation in Spetroradiometry' [ ]. Gardner's imaging scheme consists of two spherically bent mirrors whose diffraction planes are rotated by $90°$, such that the meridional and sagittal line images produced by the first mirror coincide with the sagittal and meridional images produced by the second mirror. Thus, similar to the scheme shown in Fig. 5, Gardner's scheme images a point into a point with the use of two spherical mirrors. Yet, in spite of this similarity, there are also significant differences, which we want to point out:

(1) The imaging scheme shown in Fig. 5 has a common diffraction plane for both spherical mirrors. This arrangement with a common diffraction plane is possible if one of the two *sagittal* line images is a virtual image, as shown in Fig. 5. The

parameters of the scheme R_1, R_2, θ_1, and θ_2 can then be appropriately chosen, such that the point object P and its point image I are on the Rowland circles of mirror-1 and mirror-2 and that one obtains an exact superposition of the two *meridional* line images B_{m1}, B_{m2} and the two *sagittal* line images B_{s1}, B_{s2}, respectively.

(2) By contrast, Gardner's scheme operates with two real *meridional* and two real *sagittal* line images, so that as a result the diffraction planes of the two spherical mirrors must be rotated by 90° in order to superimpose the *meridional* line image from the first mirror with the *sagittal* line image from the second mirror and, vice versa, the *meridional* line image from the second mirror with the *sagittal* line image from the first mirror. The *sagittal* and *meridional* line images are, however, not equivalent and therefore not interchangeable due to the fact that only the *sagittal* line image is a true image and the *meridional* line image is an apparent image, as the rays which form a *meridional* image point do not all pass exactly through this point (Johann error). By interchanging the *sagittal* and *meridional* line images of the two mirrors Garner's imaging scheme is in principle less accurate than the scheme shown in Fig. 5.

(3) Since the diffraction planes for the two mirrors (crystals) are rotated by 90°, Gardner's scheme is also not suitable for x-rays, since the condition (10), which assures that the Johann errors for the two crystals are equal, can only be fulfilled if the two crystals have a common diffraction plane. It is fair to say that Gardner's scheme was designed for imaging with visible light, where the Bragg condition and condition(10) do not need to be satisfied.

The arrangement, shown in Fig. 5, where the object and image points, P and I, and their associated *meridional* line images, B_{m1} and B_{m2}, are located on the two Rowland circles, has a total magnification of $M = 1$, since mirror-1 and mirror-2 provide the magnifications $M_1 = 1$ and $M_2 = 1$ and since $M = M_1 \bullet M_2$. However, other arrangements with $M > 1$ are also feasible. Motivated by the work of Podorov et al [ ], we derive, as an example, the parameters for an arrangement, where $M_1 = 1$, $M_2 > 1$, and $R_1 > R_2$, since according to

Podorov et al. it should be possible to optimize such an arrangement with respect to image distortions by minimal (experimental) adjustments of M_1. These parameters can be determined from the *meridional* and *sagittal* imaging equations (1) and (2) for mirror-1 and mirror-2, and condition (8) for the input parameters M_1, M_2, θ_2, and $\frac{R_1}{R_2}$ by the following straightforward calculations:

From condition (8), one obtains the equation

$$(11) \qquad b_{s2} - b_{m2} = b_{m1} - b_{s1}$$

where LHS (11) can be determined from the imaging equations for mirror-2 for the given values of M_2, θ_2. Since $M_1 = 1$, it follows that $b_{m1} = R_1 \sin(\theta_1)$ and $b_{s1} = -\frac{R_1 \sin(\theta_1)}{\cos(2\theta_1)}$, so that the RHS of (11) depends only on θ_1. With some additional steps (11) can be rewritten as a cubic function in $\cos^2(\theta_1)$

$$(11') \quad \cos^6(\theta_1) + \left[\frac{E^2}{\rho^2} - 1\right] \bullet \cos^4(\theta_1) - \frac{E^2}{\rho^2} \bullet \cos^2(\theta_1) + \frac{1}{4}\frac{E^2}{\rho^2} = 0$$

where $E = b_{s2} - b_{m2}$ and $\rho = \frac{R_1}{R_2}$

Rechnungen

USE Scheme in Fig. 6 for Large magnifications

Acknowledgements

We gratefully acknowledge the support of our work by the US Department of Energy, Contract Nos. DE-ACO2-76-CHO-3073, DE-FCO2-99ER54572, and DE-AC52-07NA27344.

References

(1) M. Bitter, K. W. Hill, B. Stratton, A. L. Roquemore, D. Mastrovito, S. G. Lee, J. G. Bak, M. K. Moon, U. W. Nam, G. Smith, J. E. Rice, P. Beiersdorfer, B. S. Fraenkel, Rev. Sci. Instrum. **75**, 3660 (2004)

(2) A. Ince-Cushman, J. E. Rice, M. Bitter, M. L. Reinke, K. W. Hill, M. F. Gu, E. Eikenberry, Ch. Broennimann, S. Scott, Y. Podpaly, S. G. Lee, and E. S. Marmar, Rev. Sci. Instrum. **79**, 10E302 (2008)

(3) M. Bitter, K. W. Hill, S. Cohen, S. von Goeler, H. Hsuan, L. C. Johnson, S. Raftopoulos, M. Reale, N. Schechtman, S. Sesnic, F. Spinos, J. Timberlake, S. Welcher, N. Young, and K. M. Young, Rev. Sci. Instrum. **57**, 2145 (1986)

(4) M. Bitter, H. Hsuan, J. E. Rice, K. W. Hill, M. Diesso, B. Grek, R. Hulse, D. W. Johnson, L. C. Johnson, and S. von Goeler, Rev. Sci. Instrum. **59**, 2131 (1988)

(5) J. E. Rice and E. S. Marmar, Rev. Sci. Instrum. **61**, 2753 (1990)

(6) J. Rice, F. Bombarda, M. A. Graf, E. S. Marmar, and Y. Wang, Rev. Sci. Instrum. **66**, 752 (1995)

(7) R. Isler, Phys. Scr. **35**, 650 (1987)

(8) P. Beiersdorfer et al. in present issue of JPhysB

(9) I. Yu. Skobelev, A. Ya. Faenov, B. A. Bryunetkin, et al., JETP **81**, 692 (1995)

(10) B. K. F. Young, A. L. Osterheld, D. F. Price, et al., Rev. Sci. Instrum. **69**, 4049 (1998)

(11) T. Missalla, I. Uschmann, and E. Förster, Rev. Sci. Instrum. **70**, 1288 (1999)

(12) S. G. Podorov, A. Nazarkin, E. Förster, **259**, 696 (2006)

(13) M. Bitter, K. W. Hill, S. Scott, R. Feder, Jinseok Ko, A. Ince-Cushman, and J. E. Rice, Rev. Sci. Instrum. **79**, 10E927 (2008)

(14) M. Bitter, K. W. Hill, F. Jones, and S. Scott, Journal of X-ray Science and Technology **17**, 153 (2009)

(15) H. H. Johann, Z. Phys. **69**, 185 (1931)

(16) G. S. Monk, *'Light – Principles and Experiments', McGraw-Hill, Book Company, Inc, New York and London, 1st edition (1937), p. 52*

(17) M. Bitter, M. F. Gu, L. A. Vainshtein, P. Beiersdorfer, G. Bertschinger, O. Marchuk, R. Bell, B. LeBlanc, K. W. Hill, D. Johnson, and L. Roquemore, Phys. Rev. Lett. **91**, 265001 (2003)

(18) Baonian Wan, Jiangang Li, Xianzhu Gong, Y. Shi, M. Bitter, K. W. Hill, et al., 22nd IAEA Fusion Energy Conference, Geneva/Switzerland, Nucl. Fusion **49**, 104011 (2009)

(19) S. G. Lee, J. G. Bak, U. W. Nam, M. K. Moon, J. K. Cheon, M. Bitter, and K. W. Hill, Rev. Sci. Instrum **79**, 10E317 (2008)

(20) W. Hill, M. L. Bitter, Ch. Broennimann, E. F. Eikenberry, A. Ince-Cushman, S. G. Lee, J. E. Rice, S. Scott, Plasma and Fusion Research **2**, S1067 (2007)

(21) M. Bitter, K. W. Hill, S. Scott, S. Paul, A. Ince-Cushmann, M. Reinke, J. E. Rice, P. Beiersdorfer, M. F. Gu, S. G. Lee, Ch. Broennimann, and E. F. Eikenberry, International Conference on Burning Plasma Diagnostics, Varenna, Italy 24-28 September 2007, AIP conference proceedings, Melville, New York, Vol. 988, p. 155-164

(22) K.W. Hill, M.L. Bitter, S.D. Scott, A. Ince-Cushman, M. Reinke, J.E. Rice, P. Beiersdorfer, M-F Gu, S.G. Lee, Ch. Broennimann, and E.F. Eikenberry, Rev. Sci. Instrum. **79**, 10E320 (2008).

(23) Ch. Broennimann, E. F. Eikenberry, B. Henrich, R. Horisberger, G. Huelsen, E. Pohl, B. Schmitt, C. Schulze-Briese, M. Suzuki, H. Toyokava, and A. Wagner, J. Synchrotron Rad. **13**, 120 (2006)

(24) http://www.dectris.com/sites/pilatus100k.html

(25) J.E. Rice, A.C. Ince-Cushman, P.T. Bonoli, M.J. Greenwald, J.W. Hughes, R.R. Parker, M.L. Reinke, G.M.Wallace, C.L. Fiore, R.S. Granetz, A.E. Hubbard, J.H. Irby, E.S. Marmar, S. Shiraiwa, S.M. Wolfe, S.J. Wukitch, M. Bitter, K. Hill and J.R.Wilson, Nucl. Fusion **49**, 025004 (2009)

(26) A. Ince-Cushman, J. E. Rice, M. Reinke, M. Greenwald, G. Wallace, R. Parker, C. Fiore, J.W. Hughes, P. Bonoli, S. Shiraiwa, A. Hubbard, S. Wolfe, I. H. Hutchinson, and E. Marmar, M. Bitter, J. Wilson, and K. Hill, Phys. Rev. Lett. **102**, 035002 (2009)

(27) Y. Lin, J. E. Rice, S. J. Wukitch, M. J. Greenwald, A. E. Hubbard, A. Ince-Cushman, L. Lin, M. Porkolab, M. L. Reinke, and N. Tsujii, Phys. Rev. Lett. **101**, 235002 (2008)

(28) E. S. Marmar, M. Bakhtiari, H. Barnard, et al., Nucl. Fusion **49**, 104014 (2009)

(29) J.R. Wilson, R. Parker, P.T. Bonoli, M. Bitter, R.W. Harvey, C. Fiore, K. Hill, A.E. Hubbard, J. Hughes, A. Ince-Cushman, C. Kessel, J. Ko, O. Meneghini, C. K. Phillips, M. Porkolab, J. Rice, A.E. Schmidt, S. Scott, S. Shiraiwa, E. Valeo, G. Wallace, J.C. Wright and the Alcator C-Mod Team, Nucl. Fusion **49**, 115015 (2009)

(30) L. A. Vainshtein and U. I. Safronova, At. Data Nucl. Data Tables **21**, 49 (1978)

(31) L. A. Vainshtein and U. I. Safronova, Lebedev, P. N., Institute of Spectroscopy, Report No. 2 (1985)

(32) TFR Group, F. Bombarda, F. Bely-Dubau, M. Cornille, J. Dubau, and M. Loulergue, Phys. Rev. A **32**, 2374 (1985)

(33) I. Condrea, E. Haddad, B. C. Gregory, and B. Abel, Physics of Plasmas **7**, 3641 (2000)

(34) R. E. Bell, Rev. Sci. Instrum. **68**, 1273 (1997)

(35) R. E. Bell, Rev. Sci. Instrum. **66**, 558 (1995)

(36) S. Davis, R. Barnsley, and P. Pampin, UKAEA Contract EFDA 05-1350 D5.1: ITER X-ray Crystal Spectrometry Final Report, Culham, November, 2006

(37) J. L. Gardner, Metrologia **28**, 251 (1991)

(38) http://www.edmundoptics.com

(39) D. Attwood, Soft X-rays and Extreme Ultraviolet Radiation: Princples and Applications, Cambridge University Press 1999, ISBN-13 978-0-521-65214-8

Figure Captions

Figure 1: Illustration of the imaging properties of a spherically bent crystal and the preferred experimental arrangement on tokamak experiments.

Figure 2: X-ray imaging crystal spectrometer for the observation of the spectra of helium-like argon on Alcator C-Mod. The colored traces on the three Pilatus detector modules represent different spectral lines. The wavelength and spatial information are displayed along the short and long dimensions of the detector modules, respectively.

Figure 3: Spatially resolved spectra of helium-like argon from the Alcator C-Mod discharge 1070614011. The spectra were taken at 0.917 s, during the phase with auxiliary ion cyclotron heating of 3 MW.

Figure 4: Spectra of helium-like argon as a function of time for a fixed position $z = -0.68cm$, slightly below the horizontal mid-plane of Alcator C-Mod, from the discharge 1070614011.

Figure 5: Imaging scheme with a matching pair of spherically bent crystals for the Bragg angles $\theta_1 = 35°$ and $\theta_2 = 55°$. The ratio of the radii of curvature for the two crystals is $\frac{R_2}{R_1} = 1.43$. The total magnification is $M = 1$.

Figure 6: Imaging scheme with a matching pair of spherically bent crystals for the Bragg angles $\theta_1 = 54°$ and $\theta_2 = 65°$. The ratio of the radii of curvature for the two crystals is $\frac{R_2}{R_1} = 1.39$. The total magnification is $M = \frac{\cos(2\theta_2)}{\cos(2\theta_1)} = 2.08$.

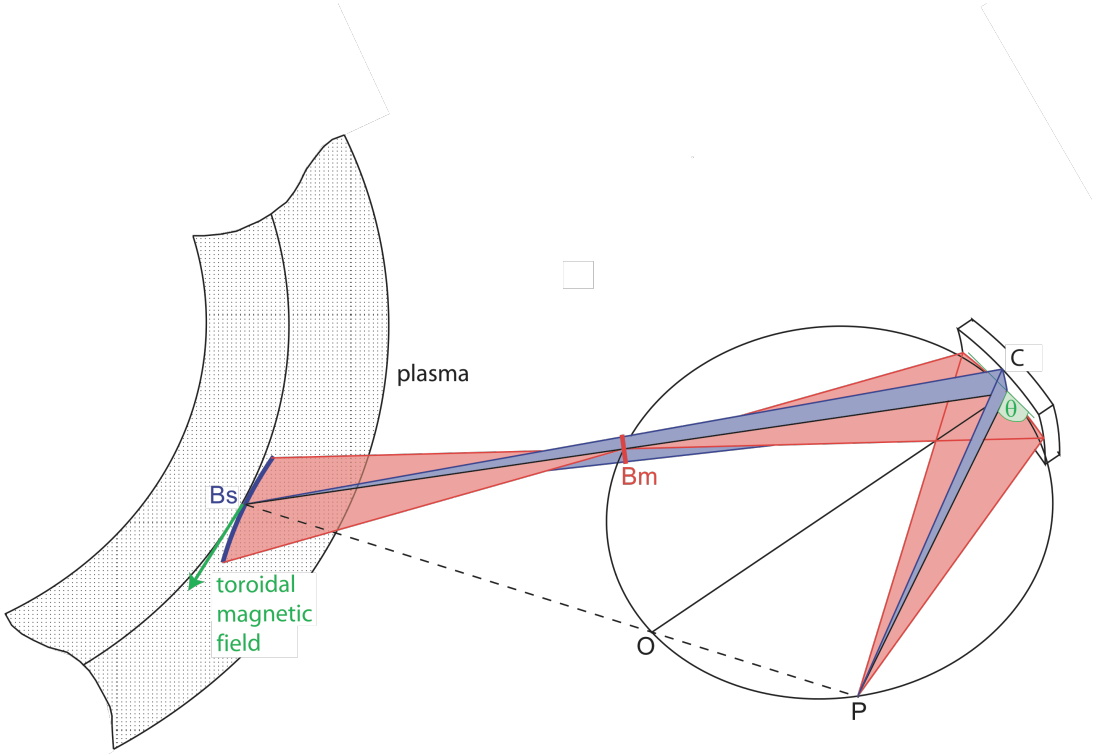

Figure 1: Illustration of the imaging properties of a spherically bent crystal and the preferred experimental arrangement on tokamak experiments.

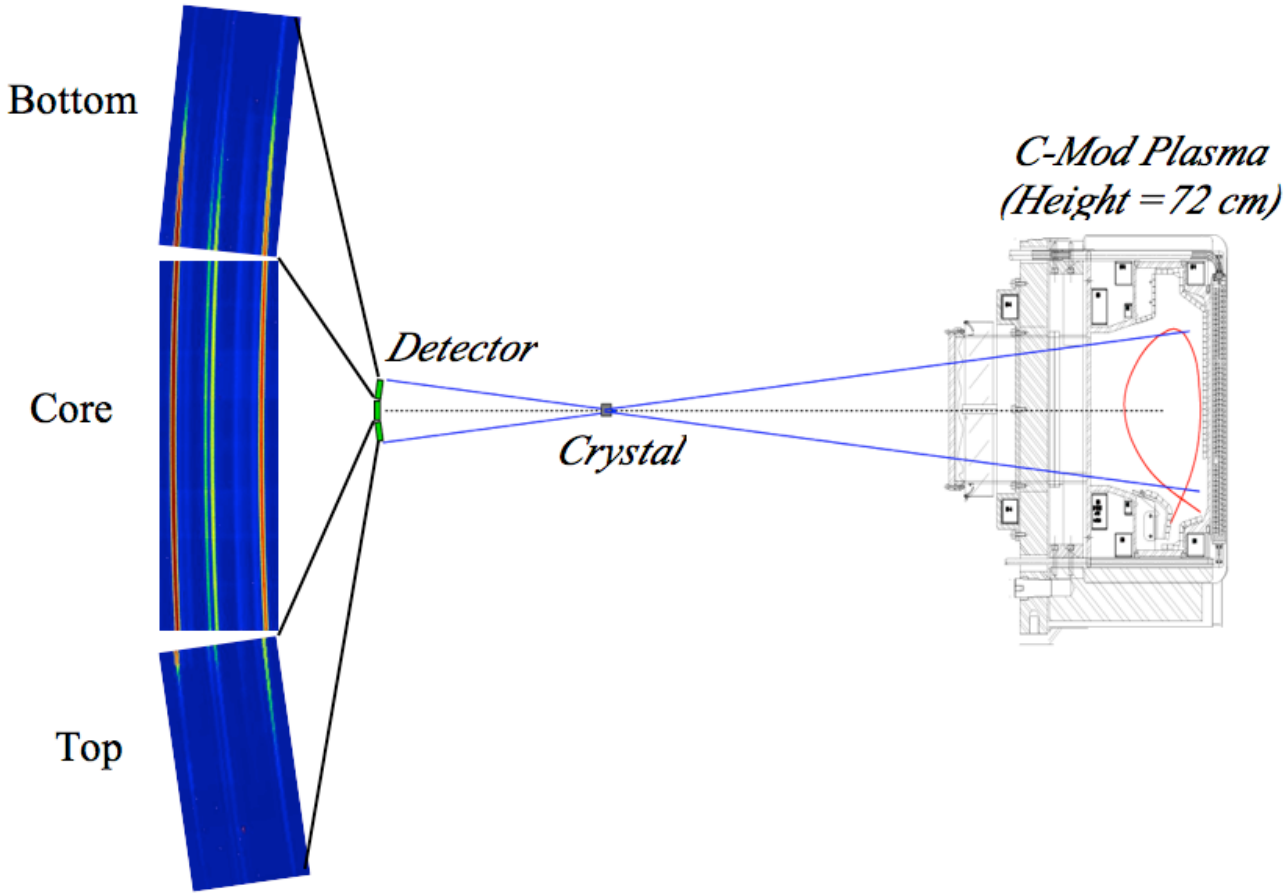

Figure 2: X-ray imaging crystal spectrometer for the observation of the spectra of helium-like argon on Alcator C-Mod. The colored traces on the three Pilatus detector modules represent different spectral lines. The wavelength and the spatial information are displayed along the short and long dimensions of the detector modules, respectively.

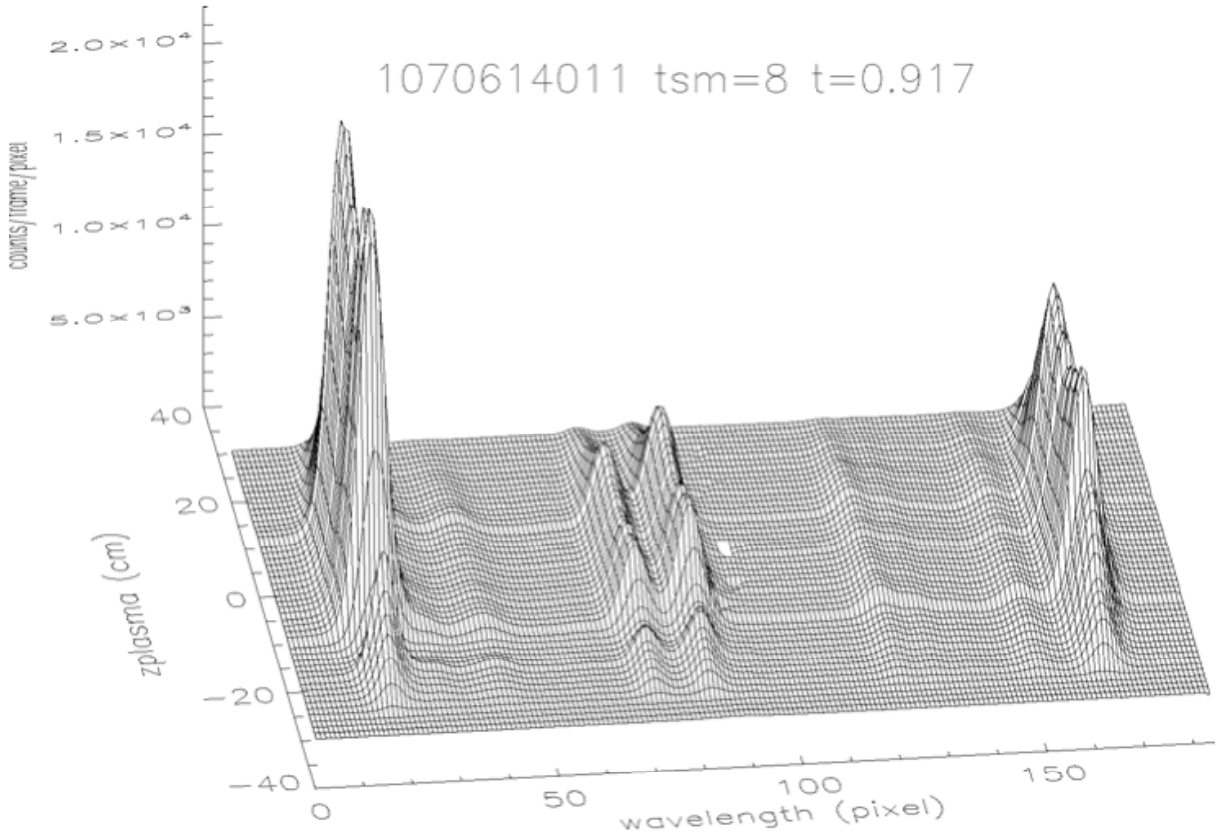

Figure 3: Spatially resolved spectra of helium-like argon from the Alcator C-Mod discharge 1070614011. The spectra were taken at 0.917 s, during the phase with auxiliary ion cyclotron heating of 3 MW.

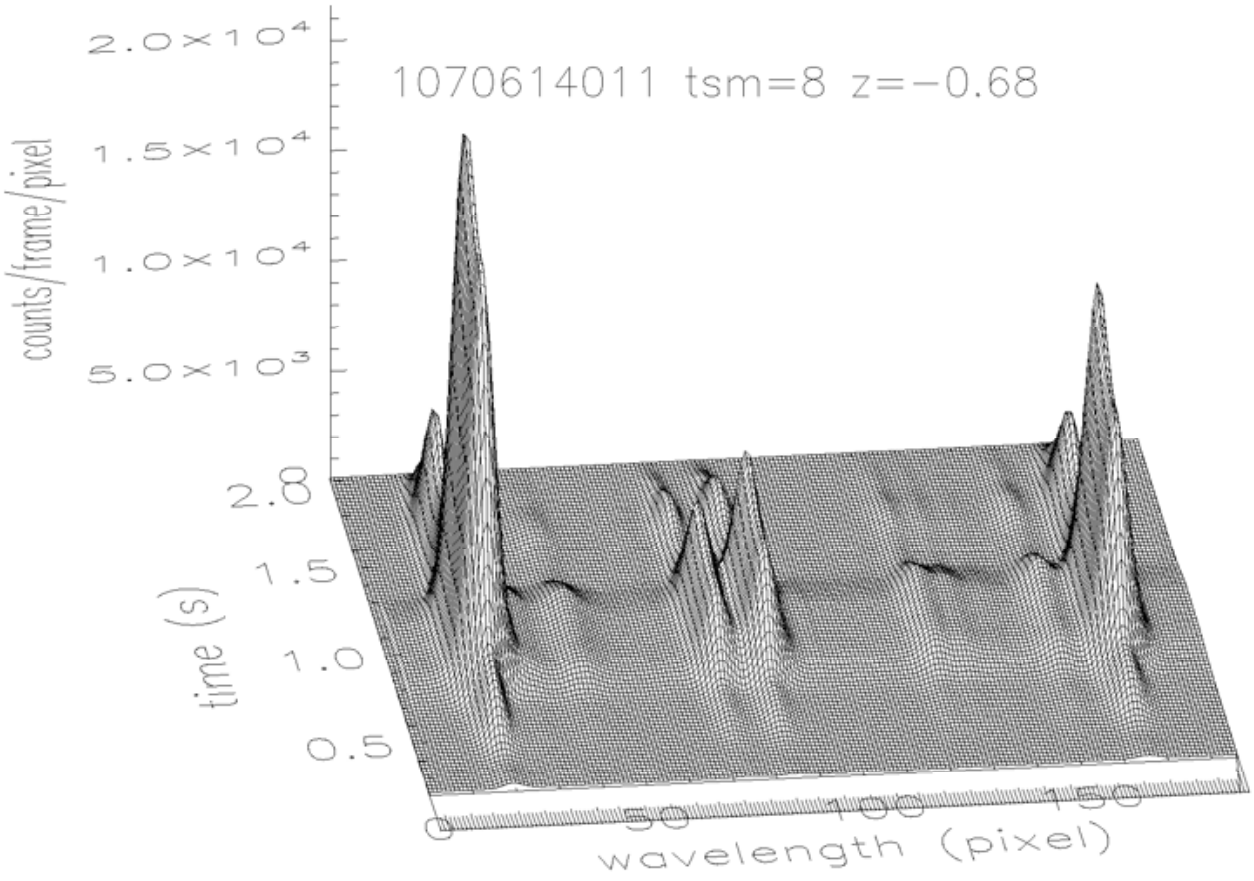

Figure 4: Spectra of helium-like argon as a function of time for a fixed position $z = -0.68cm$, slightly below the horizontal mid-plane of Alcator C-Mod, from the discharge 1070614011.

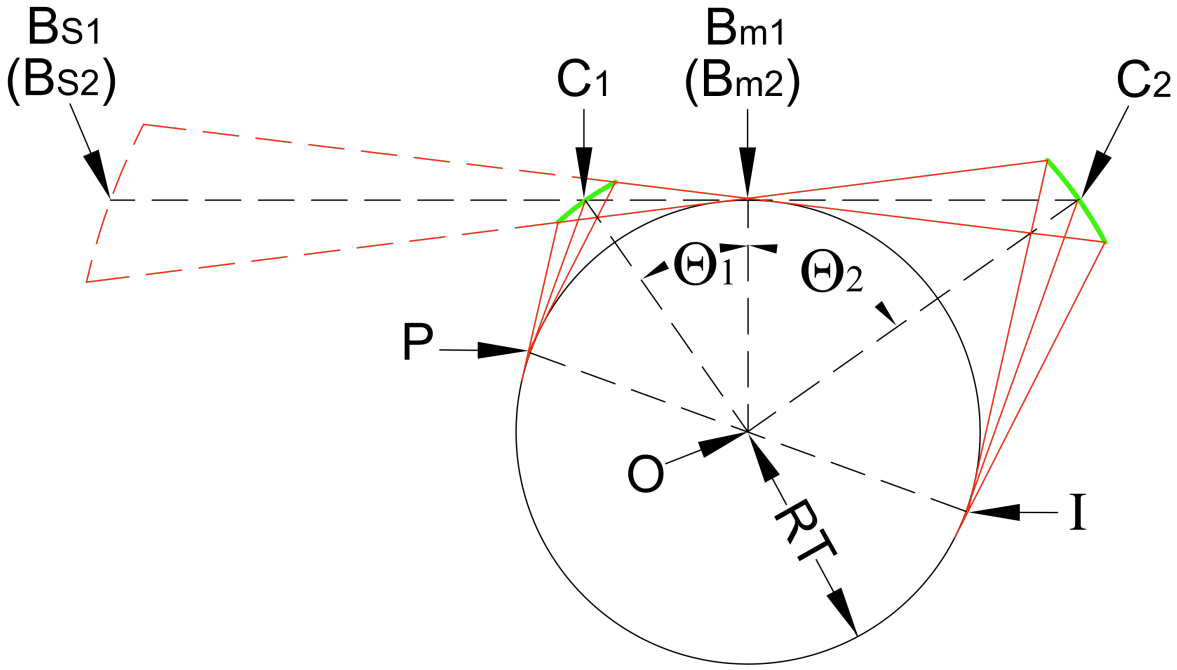
BS1
(BS2)
C1
Bm1
(Bm2)
C2
Θ1
Θ2
P
O
RT
I

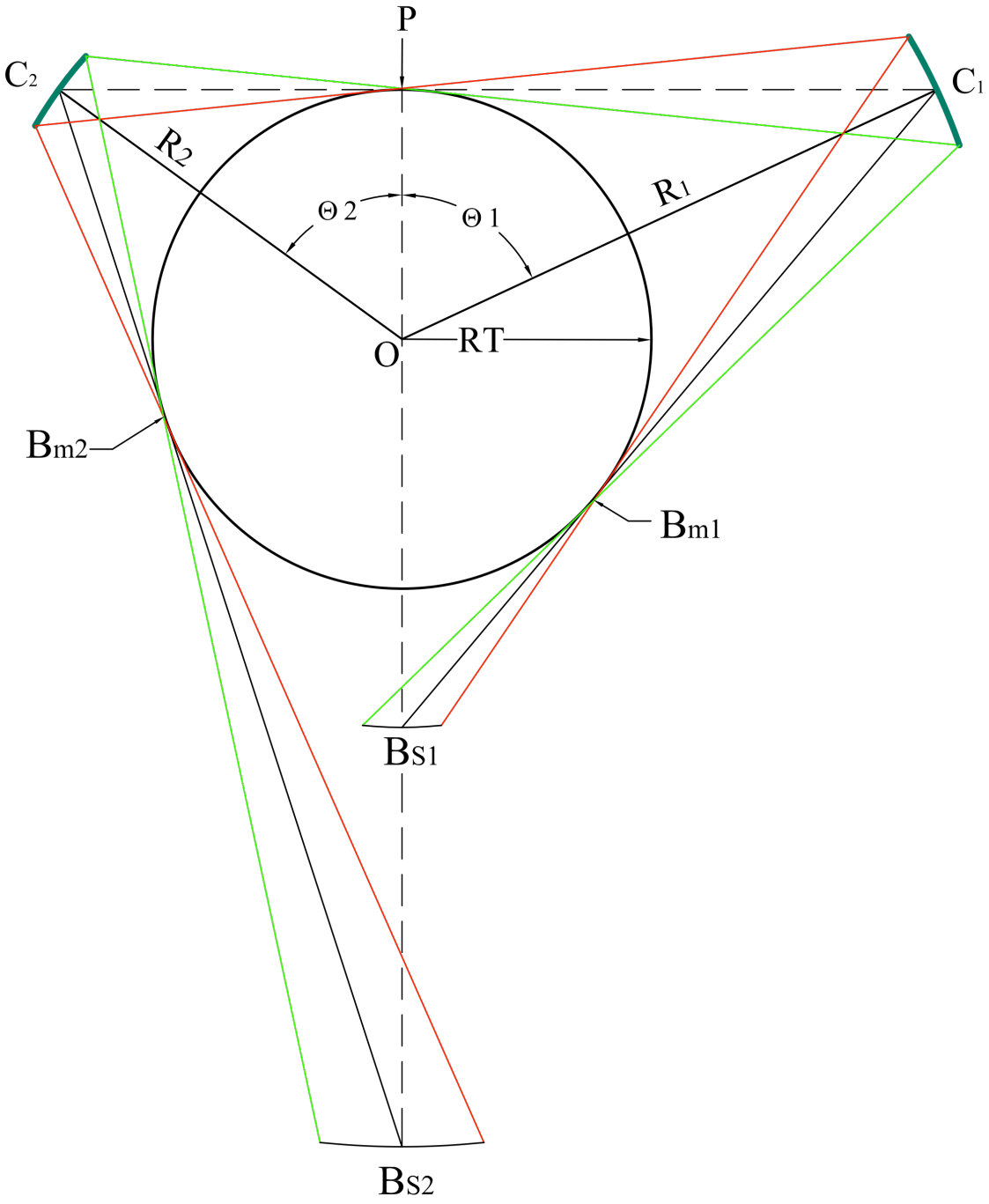
P
C2
C1
R2
R1
Θ 2
Θ 1
O
RT
Bm2
Bm1
BS1
BS2

The Princeton Plasma Physics Laboratory is operated
by Princeton University under contract
with the U.S. Department of Energy.

Information Services
Princeton Plasma Physics Laboratory
P.O. Box 451
Princeton, NJ 08543

Phone: 609-243-2750
Fax: 609-243-2751
e-mail: pppl_info@pppl.gov
Internet Address: http://www.pppl.gov